Pseudo-3D visualization of Faraday structure in polarized radio sources: methods, science use cases, and development priorities

Lawrence Rudnick,[1]* C. Anderson,[2] W. D. Cotton[3], A. Pasetto[4], E. Alexander[5], M. Tahani [6]

[1] *Minnesota Institute for Astrophysics, University of Minnesota, 116 Church St. SE, Minneapolis, MN 55455, USA*
[2] *Research School of Astronomy and Astrophysics, Australian National University, Canberra, AUS*
[3] *National Radio Astronomy Observatory, Charlottesville, VA, USA*
[4] *Institute for Radio Astronomy and Astrophysics, National Autonomous University of Mexico,Michoacán, México*
[5] *Jodrell Bank Centre for Astrophysics, Department of Physics and Astronomy, University of Manchester, Manchester, UK*
[6] *Kavli Institute for Particle Astrophysics and Cosmology, Stanford University, Stanford, CA, USA*

24 September 2024

ABSTRACT

We introduce the construction of polarized intensity cubes $\mathbb{P}$(RA, Dec, Φ) and their visualization as movies, as a powerful technique for interpreting Faraday structure. $\mathbb{P}$ is constructed from maps of peak polarized intensity P(RA, Dec) with their corresponding Faraday depth maps Φ(RA, Dec). We illustrate the extensive scientific potential of such visualizations with a variety of science use cases from ASKAP and MeerKAT, presenting models that are consistent with the data but not necessarily unique. We demonstrate how one can, in principle, distinguish between cube structures which originate from unrelated foreground screens from those due to magnetized plasmas local to the emitting source. Other science use cases illustrate how variations in the local n_e B, and line-of-sight distance to the synchrotron emitting regions can be distinguished using Faraday rotation. We show, for the first time, how the line-of-sight orientation of AGN jets can be determined. We also examine the case of M87 to show how internal jet magnetic field configurations can be identified, and extend earlier results. We recommend using this technique to re-evaluate all previous analyses of polarized sources that are well-resolved both spatially and in Faraday depth. Recognizing the subjective nature of interpretations at this early stage, we also highlight the need and utility for further scientific and technical developments.

Key words: Galaxies: active – Galaxies: magnetic fields – magnetic fields – polarization – Methods: observational

1 INTRODUCTION

Maps of the peak Faraday depth Φ[1] in a Faraday spectrum provide information on the magnetized thermal medium along each line of sight to the synchrotron emission region. When there is a single dominant Faraday depth Φ in each observing beam, $\Phi = \int n_e(\mathbf{s}) \, \mathbf{B}(\mathbf{s}) \cdot \mathbf{ds}$, where $\mathbf{B}$ is the magnetic field, and n_e is the electron density along the line of sight $\mathbf{s}$. These maps thus contain information about foreground magnetized thermal plasmas that are *unrelated* to the source, such as the Milky Way, as well as about the medium local to, or even mixed with the synchrotron emitting plasma. This paper introduces a powerful visualization technique to distinguish between these unrelated foregrounds and local media, as well as to probe the physical conditions when the Faraday medium is local to the source.

A variety of methods to display the variations in Φ for extended sources have been used. The earliest results were presented as one-dimensional plots of Φ along a source (Stull et al. 1975; Hogbom 1979). Displaying 2D Φ distributions was more challenging, and grids of numbers or symbols were used, along with contours (Dennison 1980; Perley et al. 1984a). Greyscale maps of RM were an improvement on this (Leahy et al. 1986), and finally false-color images were introduced (Laing et al. 2006) and today remain the almost exclusive type of display (see Fig. 1 here, and Knowles et al. 2022; Baidoo et al. 2023; Anderson et al. 2022). None of these methods facilitate finding correlations of Φ structures with the synchrotron structures, or even revealing spatial patterns in Φ, unless they are quite obvious, such as the bands reported by Guidetti et al. (2011).

A significant advance came with the development of Faraday Synthesis (Brentjens & de Bruyn 2005), which allowed the detection of multiple Faraday depths along the same line of sight. A cube $\mathbb{F}$(RA, Dec, Φ) is produced, where the Φ axis is the Faraday spectrum at each position. Brentjens (2011) used a $\mathbb{F}$(RA, Dec, Φ) cube of the Perseus cluster of galaxies to display results as a series of fixed Φ(RA,Dec) frames. A significant new type of display, a 2D image of Φ vs. a spatial dimension, was introduced by Pizzo et al. (2011) but has not been well-utilized in the literature. The richness of the information that could be extracted from these cubes is apparent in the animations of radio structures in Abell 194 (Rudnick et al. 2022), closely related to the technique introduced here.

In order to understand the need for more powerful forms of visualization, we briefly review how maps of Faraday depth have

---

* E-mail: larry@umn.edu (LR)
[1] This is equivalent to the "rotation measure" (RM), when there is a single peak in the Faraday spectrum, or when Φ is calculated by fitting a slope to the observed variation of polarization angle vs. wavelength-squared
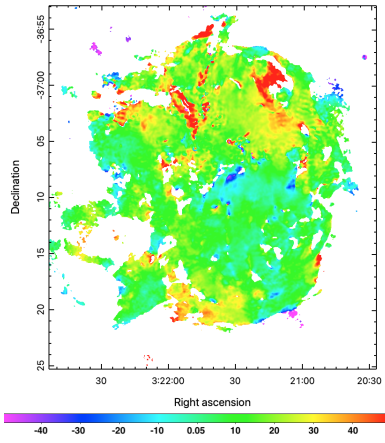
Figure 1. Peak Faraday depth image of Fornax A, western lobe, from Anderson et al. (2021).

been used. They have yielded extensive information on the structure and strength of magnetic fields in foreground screens, unrelated to the emitting source, e.g., the magnetic structure of the Milky Way (Simard-Normandin & Kronberg 1979; Taylor et al. 2009; Oppermann et al. 2015; Hutschenreuter et al. 2022), nearby galaxies (Han et al. 1998) and the intervening intracluster medium (Govoni et al. 2003). The new visualization technique introduced here does *not* add any value in these cases of unrelated foregrounds, so we turn now to Faraday structures local to the emitting source.

Local explanations for Φ variations were first reported in the early 1990s by Taylor et al. (1992) for the hot spot in 3C 194, and later, e.g., by Sebokolodi et al. (2020) and references therein, to explain extreme variations in Φ across Cygnus A spanning thousands of rad m^{-2}. Other examples of local Faraday contributions have been suggested for the depolarised patches in Fornax A (Anderson et al. 2018b), bands of low and high Φ in 0206+35, 3C 270, 3C 353 and M84 (Guidetti et al. 2011), and for other systematic Faraday patterns (e.g., Guidetti et al. 2010, 2012; Anderson et al. 2022). Recently, Jerrim et al. (2023) have used magnetohydrodynamic (MHD) simulations of active galactic nuclei (AGN) jets to develop new tools for using Faraday variations as probes of their environments.

In this paper, we introduce a new visualization technique to allow a more systematic examination of the local Faraday effects in radio galaxies. The technique itself, introduced in Sec. 2, is quite simple, creating Faraday cubes similar to the $\mathbb{F}$ cubes from Faraday synthesis, and then examining them from different angles, either manually or through animations. We then present a number of *science use cases* in Sec. 3 to first distinguish unrelated foreground from local Faraday media, and then to explore different physical connections between the synchrotron-emitting and magnetized thermal plasmas. We point out the kinds of science questions these case studies raise for further study, along with a few new science insights. In Sec. 4, we summarize the technical and scientific developments needed to make the technique more objective, robust, and powerful. Concluding remarks are made in Sec. 5 .

2 TECHNIQUE

The purpose of the technique is to look for correlations between the structures seen in polarized intensity images and the variations in Φ. In many situations, this is very difficult using the pairs of maps that are published, respectively indicating the Faraday depth,

Φ(RA,Dec), and amplitude, P(RA,Dec), of the local peak in the Faraday spectrum. In this paper, we suggest re-creating pseudo-3D cubes $\mathbb{P}$(RA, Dec, Φ) from this pair of maps, providing an additional powerful diagnostic of the underlying Faraday structure. We note that the $\mathbb{P}$ cubes lose information about complexity that is present in the full Faraday cubes $\mathbb{F}$(RA, Dec, Φ), but also gain simplicity when spurious sidelobe structures or faint Faraday components are eliminated. $\mathbb{P}$ cubes can also be constructed where the P, Φ maps were created from narrow-band multi-frequency observations and no full Faraday cubes are available.

To create the pseudo-3D cube, $\mathbb{P}$, one first chooses the range of Faraday depths Φ_1 to Φ_2 to be displayed, and the number of pixels n_Φ along the Φ axis. Each pixel k on the Φ axis corresponds to an interval $\pm \frac{\delta\Phi}{2}$ around a specific Φ_k where $\delta\Phi = \frac{\Phi_2 - \Phi_1}{n_\Phi}$. Indicating (RA,Dec) with their pixel coordinates, (i, j), yields

$$\mathbb{P}(i, j, k) = \begin{cases} P(i, j) & \text{if } \Phi(i, j) = \Phi_k \pm \frac{\delta\Phi}{2} \\ 0 & \text{otherwise} \end{cases}$$

For display purposes, it is useful to smooth along the k axis with some width Φ_{sm}, which can be used to provide some indication of the uncertainty in Φ. It is important to resist the obvious, but incorrect choice of Φ_{sm} to be equal to the width of the main peak in the Faraday spectrum, since the errors in Φ are smaller than that by a factor of 2× the signal/noise. Illustrations of the effect of choosing different values for Φ_{sm} are shown in Appendix A.

Figure 2 shows the western lobe of Fornax A. Examination of the accompanying movie which views the cubes from different angles, shows the existence of long, coherent structures in (RA,Dec,Φ) space. Such features are important for understanding the MHD behaviors of jet-inflated lobes. These structures can also be seen, partially overlapping each other, in the two projections in Fig. 2. At the top, we see the view of $\mathbb{P}$ from the top, i.e., projected along the Declination axis onto the (RA, Φ) plane. To the right, we see the view from the side, i.e., projected along the RA axis onto the (Dec, Φ), plane. These two projections are somewhat arbitrary in the sense that they do not necessarily correspond to the structure of the source. For each source under investigation, movies and interactive changes in view should be used to find the most useful projections. As shown below for our first science use case, Fornax A, features can then become apparent that are extremely difficult to recognize in other ways.

We provide a python tool to create $\mathbb{P}$ cubes from matched pairs of polarized intensity (P) and Faraday depth (Φ) maps, as described in Appendix B. Movies, such as presented here, are an essential part of looking for the signatures of different physical situations, and can be created from $\mathbb{P}$ by using $SAOImageDS9$, or other applications. In particular, we recommend use of *SlicerAstro* (Punzo et al. 2017), a powerful interactive tool for visualizing cubes.

3 SCIENCE USE CASES

We now discuss a number of science use cases to illustrate the type of information that can be extracted from $\mathbb{P}$. The scientific scope of this paper is limited to illustrating the types of information that can be extracted from $\mathbb{P}$, and why those are scientifically important.

The information derived from $\mathbb{P}$ is based on correlations between the polarized intensity structures and the variations in Φ. If no significant correlations exist, then it is likely that the Φ variations arise in an unrelated foreground screen, and there is no further information that can be derived from $\mathbb{P}$.

A hint of the (P, Φ) correlations in Fornax A can be seen in the left
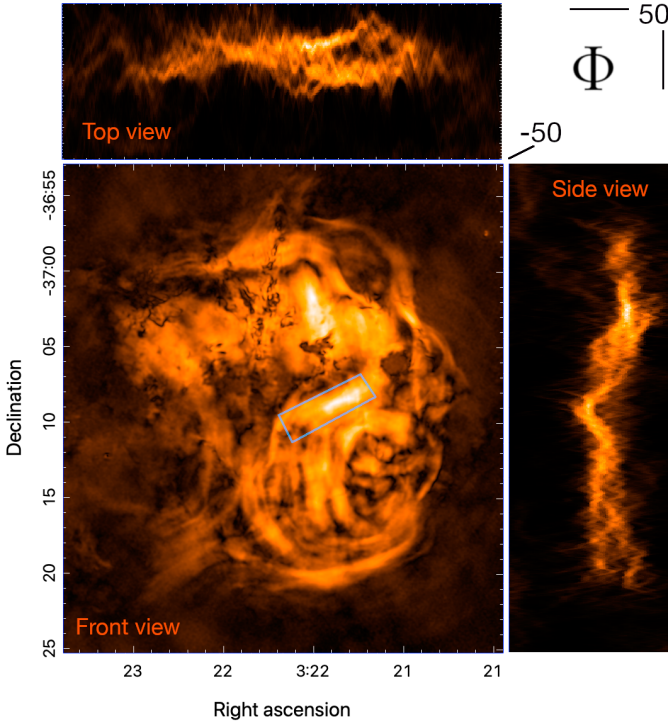
Figure 2. 2D projections of the $\mathbb{P}$ cube of the western lobe of Fornax A, from the full movie. Bottom left: polarized intensity of the western lobe of Fornax A, from Anderson et al. (2021). The feature enclosed by the cyan rectangle is discussed in Sec. 3.4.2. Top: the "top view," i.e., the projection of the $\mathbb{P}(RA, Dec, \Phi)$ cube onto the (RA, Φ) plane. Right: the "side view," i.e., the projection of the $\mathbb{P}(RA, Dec, \Phi)$ cube onto the (Dec, Φ) plane. In both images the range of Φ goes from -50 to +50 rad m^{-2}. The smoothing width is 5 rad m^{-2}. An animated version rotating through the top and bottom left panels is available in the ancillary files. The animation is 10 seconds long, and projects the cubes at viewing angles from 0 to 90 degrees around the RA axis. The Φ axis label is projected into a single position at the beginning of the animation; it becomes visible as the cube rotates.
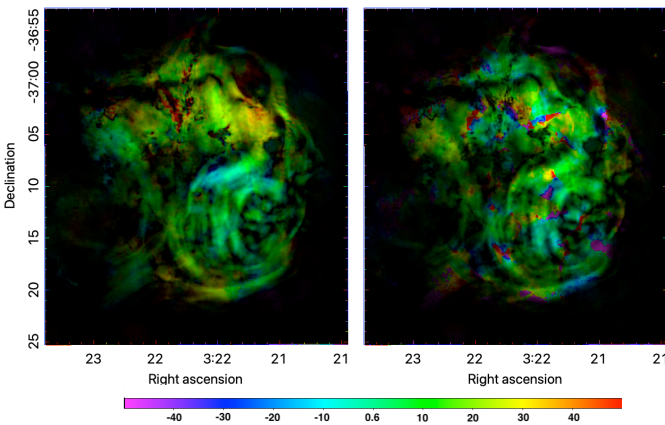

Figure 3. The same image of the Fornax A western lobe as in Fig. 1, but here with the brightness corresponding to the polarized intensity. Left: Color-coding is Faraday depth, the same as Fig. 1. Right: Color-coding using a "mock" Faraday depth distribution from the Fornax A *eastern* lobe.

panel of Fig. 3, using a different display of the same Φ map shown in Fig. 1. Here, the brightness in the image indicates the brightness of the polarized intensity map P at each position.

In the right panel of Fig. 3 is the same polarized intensity image, but this time color-coded by the Faraday depth in an *unrelated* screen (designated here as "mock"). The mock screen is formed from the *eastern* lobe of Fornax A, spatially scaled by a small factor (13%), to cover the western lobe. This "mock" Faraday screen thus has, to first order, the same distribution of Faraday depths and the same spatial scales as the true screen.[2] Most of the correspondence between polarized intensity and Faraday depth structure seems to have disappeared, which it should if the two are not related. However, given that there are significant large scale variations across the Φ map, some accidental correspondences can and do appear.

The effects seen in Fig. 3 are subtle, however, and we propose the use of $\mathbb{P}$ to better identify relationships between P and Φ. Our first science use case includes distinguishing between an unrelated intervening Faraday medium and a local one mixed with the synchrotron emitting plasma.

3.1 Case 1: Mixed thermal and synchrotron plasmas

Science context. There is a substantial literature on filamentary structure in radio lobes. van Breugel & Fomalont (1984) detected fine-scale structures in 3C 310, with high fractional polarizations. They suggested that these represented "bubble" boundaries within the diffuse lobes. Perley et al. (1984b) revealed a "wealth" of filamentary structures within the wide lobes of Cygnus A. Other suggestions of filamentary structures include the Seyfert-starburst galaxy NGC 3079 (Sebastian et al. 2019) and NGC 6068 (Candini et al. 2023). Rudnick et al. (2022) found evidence for mixed synchrotron filaments embedded in a thermal plasma in the southern lobe of 3C 40B.

Here, we examine Fornax A, whose lobes have unprecedented filamentary structures (Fomalont et al. 1989), which are polarized with lengths spanning most of the lobe. Correlations between depolarization and total intensity structures are presented in Anderson et al. (2018b). Examination of $\mathbb{P}$ gives us the opportunity to disentangle the 3D structures within these interspersed and interacting thermal and relativistic plasmas.

We use two projections from $\mathbb{P}$ to illustrate the difference in appearance between local and unrelated foreground screens, using the actual and mock Φ maps described earlier. Figure 4 presents the same face-on polarized intensity map of Fornax A West as in Fig. 2, along with two versions of the top view in (RA, Φ) space. To allow the structures arising from different regions to be seen more clearly, we color-coded the polarized intensity into three different bands. The color-coding is the same in the two "top views". In the upper "top view", from the actual or "true" Φ maps, we see the same structures that are visible in the Fig. 2 "top view", but here we can see that each color band has its own long coherent features which are even clearer in the movies.

In the lower "top view" projection, the Faraday structure is the "mock" one. In most places the structures are heavily overlapping and not cleanly separated as in the true Faraday case. This arises because the mock Faraday variations are not correlated with individual polarized intensity structures in the West lobe. Occasional features

---

[2] The similarity between the Faraday depth distributions of the two lobes is not necessarily true for all sources, so this type of experiment must be used judiciously.
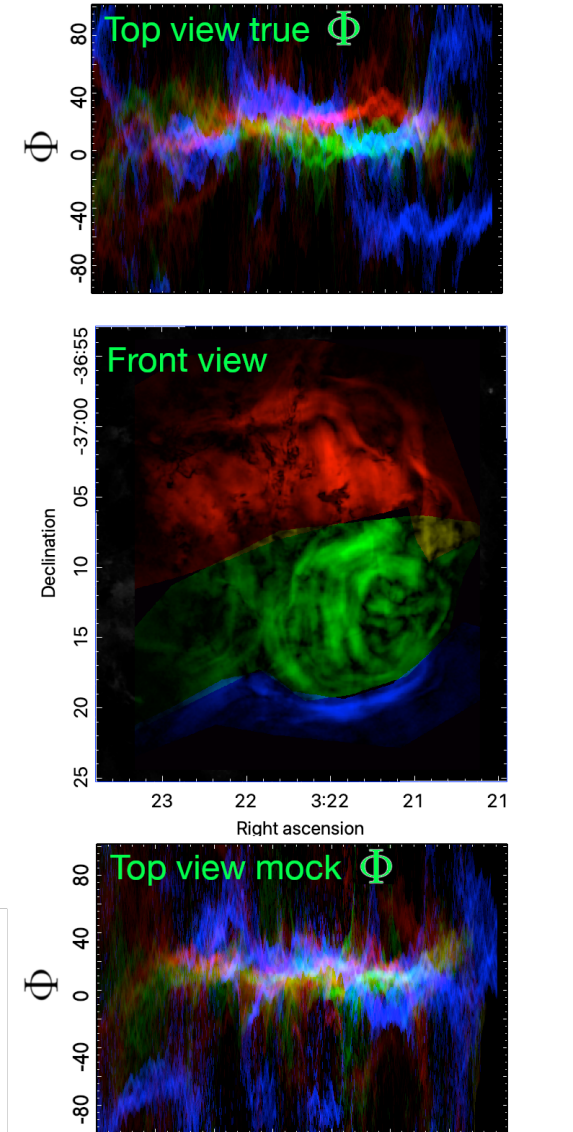
Figure 5. The $\mathbb{P}$ cube of Fornax A West viewed from an angle of 65° above the plane of the sky, and with the major axis rotated towards us by ~20° from the plane of the sky. These angles are in a 3 dimensional space where 1 rad m^{-2} = 5 ″. The axes have been stretched to preserve the RA, Dec aspect ratio.

Figure 4. Middle: polarized intensity of the western lobe of Fornax A, with colored bands to distinguish emission from different regions. Top: the "top view" showing the projection onto the (RA, Φ) plane, using the true Faraday distribution, showing an expanded Φ range from the top panel in Fig. 2, with the addition of the color information. The smoothing width is 5 rad m^{-2}. Bottom: the "top view" projection along the (RA,Φ) plane, but using the "mock" Faraday distribution.

with larger scales are seen, and are expected even at random, when the Faraday variations have large angular scales.

As discussed in more detail below, foregrounds from the Galaxy can contribute to the observed Faraday variations. Since they are unrelated foregrounds, they will not be correlated with the structures in P; when they are large enough, however, they could mask underlying correlations. Fornax A is large in angular size, but given its high latitude and anti-Galactic direction ($l = 240.2°$, $b = -56.7°$), coupled with its location to the south-west of and outside of the Orion-Eridanus superbubble, we expect a small or negligible Galactic contribution to the observed variations in Φ ($\lesssim 5$ rad m^{-2} on the scale of the lobes and below, based on an RM structure function analysis in the Fornax A region by Anderson et al. 2015).

After consideration of possible Galactic effects, the critical test
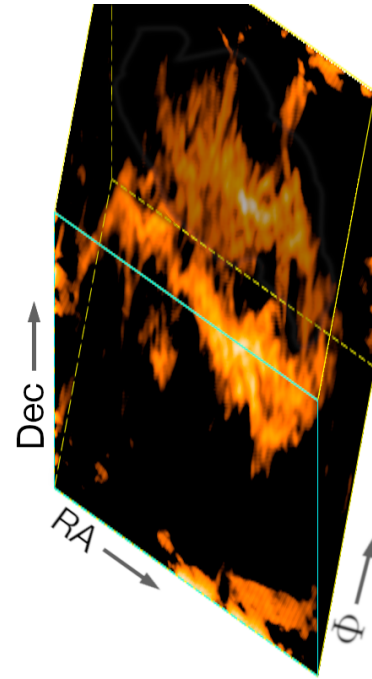
is the comparison of the true and mock views. The separation of different structures visible in the true "top" ($\Phi.RA$) view, but not in the corresponding mock view, indicates a significant correlation between P and Φ structures. This then leads us to the conclusion that the filamentary polarized structures in Fornax A West are embedded in a lobe-filling thermal plasma. It confirms and extends the suggestion by Anderson et al. (2018b) for a local thermal plasma as the cause of the depolarised patches in the lobe. The long lengths of the filaments can now be disentangled from their overlapping structures when viewed face on, and the scale sizes of the magnetic field variations in the thermal plasma can now be characterized.

Examination of the Fornax A West cube from all angles led us to a new and important insight. Around one particular angle, the scattered filaments "collapse" into two coherent parallel structures. This is consistent with the bulk of the polarized emission being located in two broad bands along the major axis, as seen in Figure 5, as opposed to being scattered throughout the volume or surface of the lobe. Most of the northern portion of the lobe, from our normal face-on view, is at higher (further) Faraday depths, while the bulk of the southern portion is at lower (closer) depths.

The existence of these polarized bands appears clear, but the scaling, and even sign of the (Φ, s) mapping is unknown; these patterns might therefore be reversed and stretched arbitrarily. The identification of these polarized emission bands shows the importance of viewing the $\mathbb{P}$ cube from all angles. In this case, finding an orientation where the emission "collapsed" into compact structures was the key; other patterns may also emerge as more sources are explored.

The above findings are based on a relatively uniform magnetic field and electron density within the lobe. Whether these are physically plausible quantitatively, as well as the implications of banded polarizations are important areas for further study.
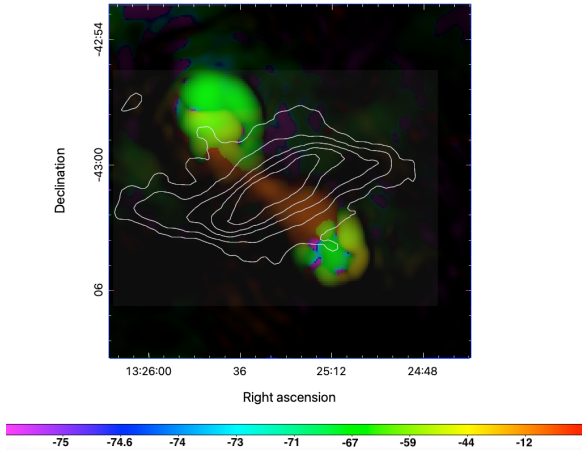
Figure 6. Polarized intensity of the inner double of Centaurus A color-coded by the local value of the Faraday depth. The contours represent the infrared radiation as observed with Herschel, starting the 3× the local rms, and each contour level increasing by a factor of 3.

3.2 Case 2: Local intervening thermal plasmas

Science context. In Case 1, the thermal plasma and the synchrotron structures within the radio source were mixed on macroscopic scales. A different situation was first discussed by Kardashev (1962), suggesting that NGC 5128 (Cen A) was interacting with a hypothetical external intergalactic medium. Interactions between outflowing synchrotron plasma and emission line material were later discussed by van Breugel et al. (1984a,b), including cases where star-formation was triggered (van Breugel et al. 1985). Through the identifications of unusual patterns of rotation measures, evidence emerged for interactions of the radio and surrounding plasmas in a number of individual radio galaxies (Carilli et al. 1988; Bicknell et al. 1990; Guidetti et al. 2010, 2011, 2012; Rudnick & Blundell 2003; Anderson et al. 2018b, 2022). Magnetic draping, (e.g. Adebahr et al. 2019, and references therein), illustrates another type of Case 2 situation, where the thermal material surrounding the radio emitting structure can be studied. More recently, Mahatma et al. (2023) suggested a connection between the bases of the lobes in 3C 34 and 3C 320 and dense regions of the surrounding thermal medium.

The inner structure of Centaurus A was mapped by Burns et al. (1983) showing a ∼15 kpc double source connected by jets, roughly perpendicular to the galaxy's dust lane. Figure 6 shows the polarized intensity of this double, color-coded by the Faraday depth, using the ASKAP commissioning data reported in Anderson et al. (2018a). The jets and transition regions into the hotspots have a Faraday depth of ∼ −26 rad m^{-2}, while the two hot spots have values near −61 rad m^{-2}, which is the same as the local Galactic foreground (Hutschenreuter et al. 2022). Galactic foregrounds are thus not likely to significantly affect these results.

Although the jets and hotspots are continuous in space, the transition between the jet and hotspot Faraday depths is sharp and ∼ 10× larger than any variations within the hot spots. The distance along the line of sight, s, cannot be changing abruptly, since the jets and hotspots must be physically connected, Since $\Phi = \int n_e(\mathbf{s}) \, \mathbf{B}(\mathbf{s}) \cdot \mathbf{ds}$, the discontinuity in Φ must arise in variations of $n_e B$ along the line of sight. The discontinuity is also seen dramatically in the top panel of Fig. 7, showing the Faraday depth Φ as a function of position along the major axis. As seen in Fig. 6, Cen A's dense molecular disk (e.g., Quillen et al. 1992) is the obvious source of the excess Faraday rotation.
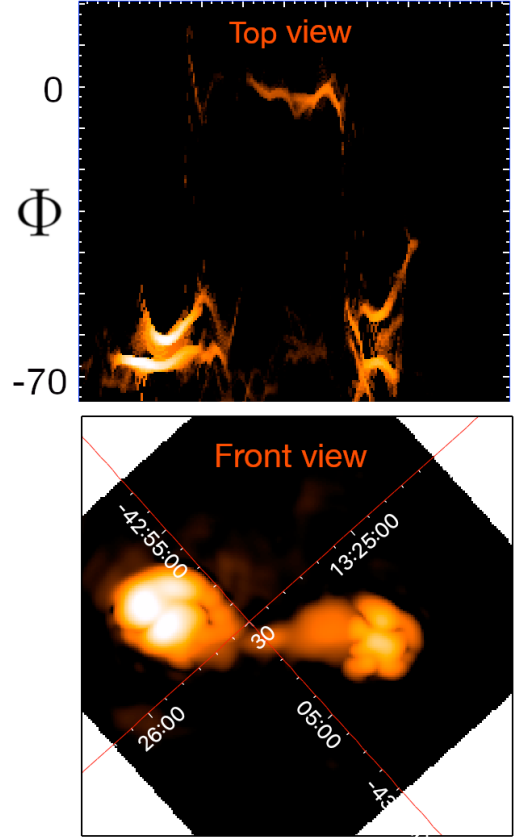

Figure 7. Bottom: Polarized intensity of the inner double of Centaurus A. Top: The "top" view in the Φ vs. position along the major axis, with the spatial scale identical to the bottom panel. The smoothing width is 2.5 rad m^{-2}. An animation rotating through the top and bottom panels is available in the ancillary files. The animation is 10 seconds long, and projects the cubes at viewing angles from 0 to 90 degrees around the major axis.

In Case 2 situations, the information from the Faraday depth variations can then be used to derive physical properties of the intervening medium, or to check for consistency with existing models. Although detailed modeling is beyond the scope of this paper, we note that the inferred change in $n_e B$ could arise if the AGN and jets were physically located at the center of Cen A's dense molecular disk (e.g., Quillen et al. 1992); the axisymmetric spiral magnetic field in the disk (Lopez-Rodriguez 2021) would then provide the necessary line of sight component to produce Faraday rotation.

In Figure 7, there is also a distinct double structure in Φ for each of the hotspots. These double structures arise from the gradients in Φ along the minor axis, which can also be seen in the closeup view in Figure 8. This pattern is easily seen in the movie which rotates the viewing angle of the $\mathbb{P}$ cube around the major axis. This is consistent with what would be expected from a toroidal component to the hot spot fields, with magnetic fields pointing towards us at the top (above the major axis), and away from us below the major axis. It is similar to what is seen in other powerful radio sources with overpressured lobes (Anderson et al. 2022).

The south-western hotspot also has a thin leading edge, (see Fig. 8) with a distinct pattern of Faraday structure which we first spotted in a high-resolution movie. The most positive values of Φ (relative to galactic) are seen at its apex, with values symmetrically decreasing away from this position. This hotspot was shown to be surrounded by a thin shell of X-ray emitting material (Figure 1 in Croston et al.
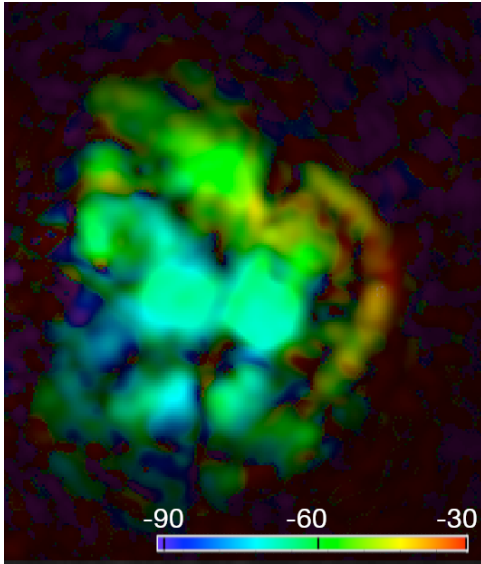
Figure 8. High resolution (10") polarized intensity of the southwestern hotspot/lobe of Centaurus A, color-coded by the Faraday depth, Φ, as shown in the colorbar in units of rad m^{-2}.

2009)[3]. Kraft et al. (2007) and Croston et al. (2009) identify the radio hotspot as the contact discontinuity driving a strong X-ray shock into the ISM. The Faraday patterns at the leading SW edge (Fig. 8) appear consistent with this, although detailed modeling is required.

3.3 Case 3: Revealing 3D structures

<u>Science Context.</u> Determining the 3D structures of radio sources, along with their line of sight orientations, is one of the biggest challenges in understanding their physics. Rotational symmetry along the major axis of straight sources has been built into models, from the earliest (Burns & Christiansen 1980) to the more recent ones (Hardcastle 2018). On scales of $10^2 - 10^3$ kpc, the effects of line-of-sight orientation in classical doubles and more recently, for HyMORs sources with terminal hot spots on only one side, have also been of interest (Saikia et al. 2003; Ceglowski et al. 2013; Harwood et al. 2020; Saikia 2022). For more complicated bent sources, 3D models of e.g., precession (Nolting et al. 2023) or orbits (Klamer et al. 2004; Gendron-Marsolais et al. 2021) are often invoked. One major tool in orientation studies has been the asymmetry in depolarization of the near vs. far lobes in a thermal galactic halo, (Garrington et al. 1988; Shah & Seta 2021); this is complicated by asymmetries in lobe lengths or in the depolarizing medium (e.g., Pedelty et al. 1989)

A special case of 3D studies is the line-of-sight orientation of jets; on pc scales, these have been studied using circumstellar obscuration and relativistic beaming, including superluminal motions (Bridle & Perley 1984; Urry & Padovani 1995; Cohen et al. 2007). The orientation of these smaller-scale jets with respect to their large-scale structure provides fundamental information about long-term stability, possible influences of black-hole mergers, and precession of the jet axis. A recent study by Ubertosi et al. (2023), e.g., finds that misalignments from the largest scale structures are quite common on pc-scales, with timescales ranging from $1-10$ Myr. X-shaped sources are a particularly interesting case, because jet precession provides a possible explanation (Dennett-Thorpe et al. 2002).

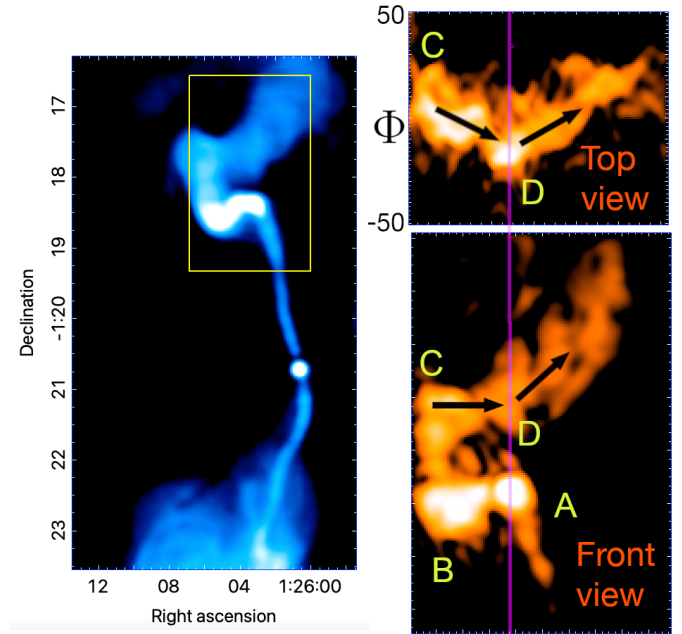[3] also see ESO's beautiful radio/optical/X-ray composite image.

Figure 9. Left: Polarized intensity of the central region of 3C40B, from Rudnick et al. (2022). Right: Zoom in on region in yellow box. Bottom panel is the same front view of polarized intensity. Top panel is the "top" view of polarized intensity in the (Φ, RA) plane, covering the final bend in the northern jet. At the location of the purple line, the jet changes direction in the plane of the sky (bottom), and the Φ gradient reverses (top). The smoothing width is 5 rad m^{-2}. An animation rotating through the top and bottom right panels is available in the ancillary files, with viewing angles from face on to 90 degrees (the top view).

3.3.1 Case 3a: Jet Bending

Our first example of identifying 3D structures relies on the comparison between a) the inferred jet flow trajectory in the plane of the sky, with b) the pattern of variations in the accompanying Faraday depths. Fig. 9 shows the inner portion of the radio galaxy 3C40B in the cluster Abell 194 (Rudnick et al. 2022). As argued there, the northern jet in this source goes through three sharp bends, at A, B, and C, likely the result of an encounter with a dense cloud in the ICM. After the last sharp bend, the jet expands and slowly changes direction (from W to NW) at the position D, marked with the vertical purple line in Fig. 9. As the jet crosses this line, it continues to expand and fade, and the change in direction in the plane of the sky is accompanied by a change in the gradient of Faraday depth. Before D, Φ decreases along the jet; after this point, Φ abruptly increases.

If there were a dense region in the ICM at location D causing the jet to bend in the plane of the sky, this would also cause a *discontinuity* in Φ, which we do not observe. Instead, Φ is observed to be continuous, while its *gradient* changes at D. This is consistent with a change in direction of the jet flow along the line of sight, at the same location where a change in jet direction is seen in the plane of the sky.

Because we do not know the local value of $n_e B$, we cannot directly calculate the scaling between Φ and s, the distance along the line of sight. However, we can check the plausibility of this picture by assuming that the trajectory changes by approximately the same angle along the line of sight that it does in the plane of the sky, $\sim 45°$. Following the prescription of Rudnick et al. (2022) leads to a line of sight magnetic field of $1.4\mu G$, with uncertainties of order unity. This

is consistent with expectations of magnetic fields in clusters, so the changing line-of-sight scenario is plausible in this case.

As in the case of Fornax A, by viewing the cube over the full range of angles, we found that the region of the 3C40B northern jet from B to C "collapsed" into a thin curvy vertical line when viewed from an azimuthal angle of $43°$ towards the west from the line of sight, in the 3D space where $1\ \mathrm{rad\ m^{-2}} = 1''$. This is consistent with the jet flattening into a ribbon-like shape for this portion of its trajectory, perhaps during its deflection by a denser region. The other portions of the jet did not indicate such flattening.

3.3.2 Case 3b: Jet orientation

Our second example of 3D information involves the line of sight orientation of the jets near an AGN, based on their Faraday variations. Fig. 10 shows three idealized situations for the magnetic and density structures in the surrounding galactic thermal medium. These are not physically accurate, but illustrate the basic observables associated with different parameters. We assume in each case that the Faraday depth at the nucleus is Φ_0 and that any unrelated foregrounds have been subtracted; in this case, the sign of Φ_0 tells us the direction of the magnetic field around the jet.

In the top example, $n_e B$ is constant throughout the region where the jets are found. Although this simplistic case is unlikely, we include it to illustrate the basic expected Faraday patterns. Because the jet is tilted with respect to the line of sight, $|\Phi|$ increases (decreases) with distance from the nucleus for the receding (approaching) jet.

The middle example represents the case where $\boldsymbol{B}$ is constant in magnitude, but switches direction at the nucleus; for simplicity, we show the case where $\Phi_0 = 0$. Such large-scale discontinuities in field directions in a galactic halo have been observed, e.g., in NGC 4631 by Mora-Partiarroyo et al. (2019). The key signature of a field reversal is a large discontinuity in Φ somewhere along the structure. Here, in the special case where the field reversal occurs across the plane of the galaxy, the receding (approaching) jet will show an increase (decrease) in $|\Phi|$ with increasing distance from the nucleus.

A more interesting and realistic case is shown at the bottom, where $n_e B$ decreases in magnitude with distance from the AGN. For the approaching jet, $|\Phi|$ drops monotonically, because of both the decreased path length along the line of sight and the lower magnitude of $n_e B$. For the receding jet, there are two opposing effects; the increased path length with distance from the AGN leads to an increase in $|\Phi|$, while the lower magnitude of $n_e B$ causes it to decrease with distance from the nucleus. On the receding side, $|\Phi|$ therefore rises and reaches a maximum at some distance from the AGN, and then decreases.

We now apply this type of analysis to PKS 2014-55, a 1.6 Mpc long radio galaxy associated with the Seyfert 2 galaxy 2MASX J20180125-5539312, at a redshift of 0.0606. PKS 2014-55 has been previously mapped using MeerKAT at a frequency of 1.3 GHz (Cotton et al. 2020a), and we use those data in this analysis.

As seen in Figure 11, the Faraday depths show only small variations on large scales, with a mean value of $45\ \mathrm{rad\ m^{-2}}$. The Galactic foreground in this direction, is $\sim +45\pm5$, so there is little net contribution from the *large-scale* environment of the radio galaxy. However, a wider range of Faraday depths is seen in the small-scale structures around the location of the host, while their mean is similar to that of the extended lobes. The double radio core structure probes the medium on the scale of $\sim$25 kpc from the AGN, where the ISM and potential halo of the host likely dominate.

No total intensity or polarized radio core is seen exactly at the position of the host galaxy, so we assume that the two slightly resolved
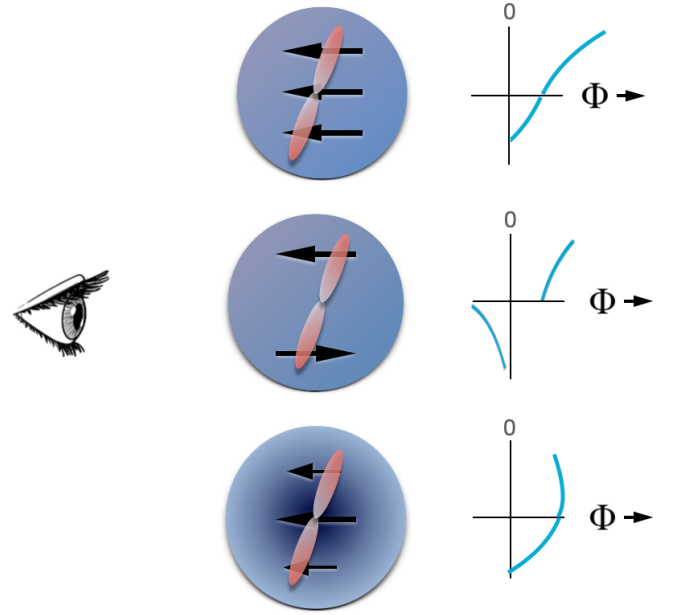

Figure 10. Illustration of Faraday depth along pair of jets for various configurations of thermal density and magnetic field.
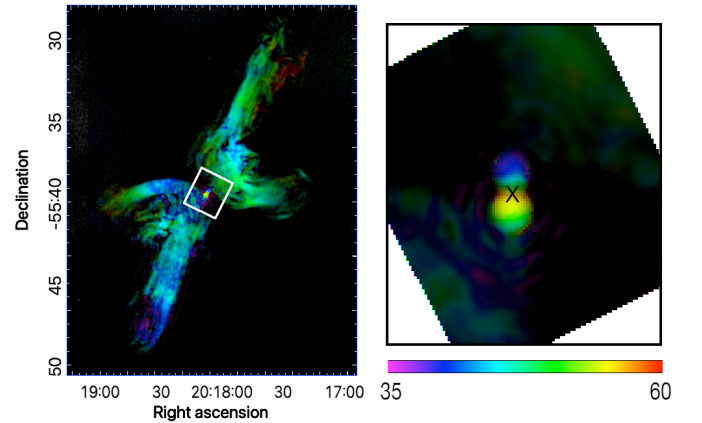

Figure 11. PKS2014-55 in polarized intensity from Cotton et al. (2020a), color-coded by Faraday depth, using the same colorbar for both frames. The right frame is rotated and zoomed in on the white box shown on the left. The host galaxy, at 20:18:01.286, -55:39:31.6, is marked with an X.

radio components straddling this position are either jets or an inner double. The significant Faraday structure in these jets can be seen in the side view of Fig. 12 and in the accompanying movie. The NW jet's depth is the same as that of the lobes and their "wings", while the SE jet depth extends to larger Φ values. This is consistent with the NW jet emerging in front of the thermal emission in the core, while the Faraday depth to the SE jet increases away from the core, peaking a few arcsec to the south, as seen in Fig. 13. With the assumptions of a uniform field direction near the host, the NW jet would then be approaching us, and the SE jet, receding.

To model this more quantitatively, we examine the Faraday depth along the major axis of the double structure (Fig. 13). The lack of a monotonic trend in Φ rules out the scenario in the top panel of Fig. 10. It also rules out the scenario in the middle panel, where the
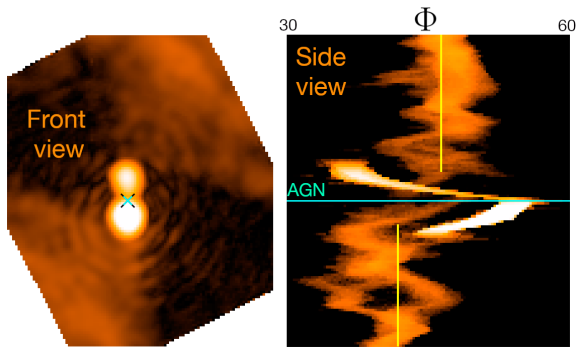
Figure 12. Polarized intensity of the central region of PKS 2014-55 rotated so that the inner double is vertical. Left: Front view, in the plane of the sky. Right: Side view, showing the variation of Φ along the major axis. The smoothing width is 2.6 rad m^{-2}. An animation rotating through the left and right panels is available in the ancillary files. The animation is 10 seconds long, and projects the cubes at viewing angles from 0 to 360 degrees around the major axis.

magnetic field switches direction across the core, because no large jump is observed.

The data are consistent, however, with the bottom panel, where $n_e B$ is highest at the center, as expected physically, and where B maintains the same orientation throughout. This leads to the observed offset peaked pattern in Φ (Fig. 13); the plotted data are accompanied by several models of a tilted jet embedded in a centrally peaked thermal plasma. It confirms the new result that the NW lobe is approaching us. and that the field is pointed towards us. This is also consistent with the expectations from the larger scale emission, since the average value of Φ in the small double is +14 rad m^{-2} above that of the lobes. The Φ pattern would be negative, mirror reflected, if the sign of the magnetic field were reversed.

With a more physically realistic model of the thermal medium density and magnetic field, it would be possible to use these results to constrain the relationship between the tilt angle and the radial extent of the medium. Additional modeling of the large-scale Faraday structure would be useful to confirm the conclusions of Cotton et al. (2020b) that the offset "wings" are likely due to deflections of the backflow, as opposed to precession of the jets.

3.4 Case 4: Jet internal magnetic field structure

Science context. In the above cases, the thermal and synchrotron emitting plasmas were either completely separated or interspersed, but not mixed on microscopic scales. In those cases, the magnetic fields can be quite different in the two plasmas. In other situations, thermal plasma can be *fully mixed* with the relativistic plasma, so that the Faraday depth depends on the same magnetic field that gives rise to the polarized synchrotron radiation. Such mixed plasmas can be difficult to detect, because the "internal", broadened Faraday structure results in depolarization that cannot be reduced using narrower bandwidths or higher angular resolutions.[4]

When jets can be resolved transversely, their 2D magnetic field configurations can be studied. At pc scales, e.g., the MOJAVE survey

[4] For broadened Faraday spectra, the parameter W_{max} indicates when the sensitivity drops by a factor of two (Rudnick & Cotton 2023). W_{max} ranges from ~150 rad m^{-2} for VLASS (Lacy et al. 2020) to only 0.5 rad m^{-2} for the LOFAR HBA (van Haarlem et al. 2013). W_{max} is much smaller than the commonly used values of "Faraday width" (Brentjens & de Bruyn 2005).
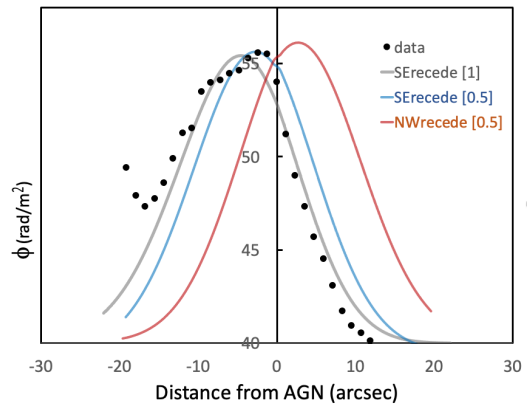
Figure 13. Faraday depth as function of angular distance from the host for PKS 2014-55. Negative numbers along the horizontal axis are to the SE. The observed behavior is similar to that in the bottom panel of Fig. 10, with the peak Faraday depth in the receding, SE, lobe. The distance of the peak from the core depends on the ratio of $sin(\theta)$ (the angle of the jets to the line of sight) to the half-power half-width of the Faraday depth assumed to be a 2D Gaussian distribution. Two models differing by a factor of two in their half-widths are labeled as [1] and [0.5]. The model also includes an amplitude normalization for Φ, reflecting the unknown magnitude of $n_e B$.

(Hovatta et al. 2012a) found four examples of transverse Φ structure, providing early evidence for the presence of toroidal or helical fields; such geometries are now well-established (Gabuzda 2021; Gómez et al. 2022). However, simulations of such gradients by Hovatta et al. (2012b) show that spurious features can result, but that they essentially disappear when the jet is at least two beams wide, and the signal:noise is $> 3\sigma$ along the observed gradient.

Spine-sheath structures can also be observed on these scales (Saikia 2022). Moving to kpc scales, there is sufficient resolution in some cases to resolve the projected, transverse structure of their magnetic fields. Laing & Bridle (2013a) describe the observed magnetic field geometries and their connection with the inferred velocities as jets undergo regions of expansion. In NGC 315, for example, Laing & Bridle (2013b) find that the fields evolve into a toroidal structure along the jet edges with a central poloidal component.

This combination of poloidal and toroidal components is also reflected in the helical magnetic field configuration in M87 (Pasetto et al. 2021). Here, the *emissivity* also shows the double helical pattern, perhaps sustained by Kelvin-Helmholtz instabilities. They also used Faraday rotation variations across the jet to illuminate the fields' line of sight components, supporting the presence of the toroidal component. In this paper, we probe additional details of M87's magnetic field structure using the $\mathbb{P}$ analysis.

3.4.1 Magnetic field structure in the M87 jet

The polarized and Faraday structures of M87 (Fig. 14), are based on the high frequency and high resolution analysis of Pasetto et al. (2021). The median value of Φ across the jet at each location shows smooth variations along the jet, covering a large range ($\lesssim 1000$ rad m^{-2}, see 2nd panel in Fig. 14). The largest excursion is in the region around bright Knot C, where the jet also undergoes a sudden bend. This correspondence between the bend and the large change in Faraday depth makes it likely that the variations are local to M87, as opposed to an unrelated foreground screen. Within the area covered by the M87 jet ($\sim 3'$ at $l = 284°$ and $b = 74.5°$), the Galactic contribution to the observed Φ variations is negligible, as
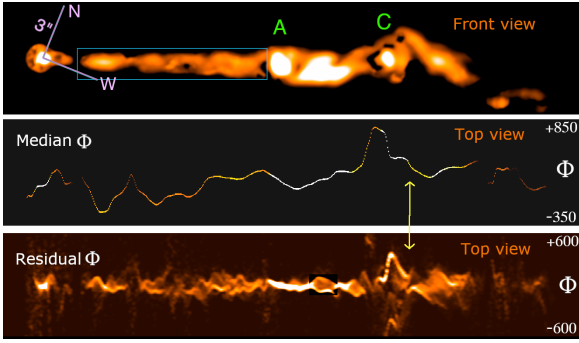
Figure 14. Polarized emission of the M87 jet, from Pasetto et al. (2021), using the 18GHz bandwidth data from C to Ku Bands, 0.43" resolution. Top: Polarized intensity, in the plane of the sky, rotated by -22°. Middle: Median value of Φ across the jet at each location along the jet. The brightness corresponds to the local polarized intensity. Bottom: Top view of the ℙ cube, constructed after removing the local median Φ value. The smoothing width is 25 rad m^{-2}. The cyan box shows the location of the "conical" jet region discussed further below. The yellow arrows indicate a discontinuity in the median and residual Faraday depths. An animated version rotating through the top and the bottom panel is available in ancillary files. The animation is 10 seconds long, and projects the cubes at viewing angles from 0 to 90 degrees around the major axis.

the region is at high latitude and no star-formation activity is present that could cause noticeable variations.

Pasetto et al. (2021) observed significant depolarization even at the relatively high frequencies of 4 GHz[5]. This likely results from the large Faraday widths within each beam, of ~ 300 rad/m^2 in the "conical" region of the jet near the core and $\sim 10^3$ rad m^{-2} further out. A thermal plasma mixed with the synchrotron emitting jet would cause such high values.

In order to explore the mixed thermal/synchrotron plasma, and the jet's internal magnetic field structure, we remove the mean variations along the jet, and look at the *residual* Φ, i.e., the variations in Φ *across* the jet at each location. Pasetto et al. (2021) used these Φ gradients to infer a double helical magnetic field structure in M87, extending out to ~ 1 kpc from the nucleus. The third panel in Fig. 14 is the "top view" of the median-Φ-subtracted Faraday cube; in most locations there is a significant range of Φ values across the jet. This is consistent with the expectations for a toroidal (helical) field component.

3.4.2 Faraday cross-sections of jets

To probe the magnetic structure *within* a jet we need a different visualization scheme. It is useful to focus on the "side view" (Y, Φ) looking down the major axis of the jet, where Y is the position transverse to the jet axis. Fig. 15 illustrates the expected results for (Y, Φ) for some simple internal magnetic field geometries.

As we turn to a more detailed structural analysis of a jet, it is important to recognize that none of the models presented in this paper are unique. There is no procedure which maps a set of observations onto a single physical model. Cartoon models are important, however, to check for consistency with the observations.

There are some important further caveats. In the discussion below, the patterns shown for these ideal cases represent the overall expected trends; the Φ values are characteristic of the *average* Φ along each
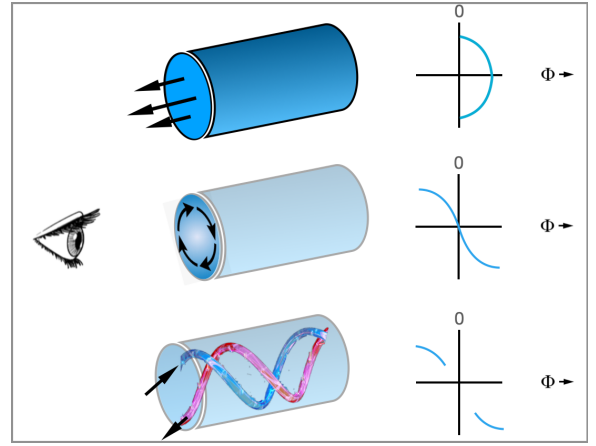
Figure 15. Cartoon showing the "characteristic" expected behaviors of Φ as a function of the distance along the projected minor axis of a jet or filament, for three simple magnetic field geometries. The Φ axis is with respect to the local foreground Faraday depth. Top: poloidal; Middle: toroidal; Bottom: toroidal, but confined to a double-helical structure. In either the toroidal or double-helical configurations, the gradient in Φ may be offset by an unsubtracted mean background.

line of sight, not necessarily its value at the peak polarized intensity. That value depends on the actual emissivity profile of the jet as a function of radius and the detailed magnetic field geometry. The cartoons represent a starting point for more detailed modeling.

Recognizing these caveats, we first consider the contribution from a poloidal field at a slight angle from the plane of the sky. For a uniform field strength, B, and constant electron density, n_e across the jet, the (absolute) Faraday depth will be largest along the axis, and decrease to the edges because of the shorter path lengths (Fig. 15, top panel). The exact shape depends on the behavior of $B(r)$ and $n(r)$, where r is the distance from the axis.

In the presence of toroidal fields, (bottom two panels of Fig. 15), there is a characteristic quasi-linear trend in $\Phi(Y)$, whose exact shape again depends on $B(r)$ and $n(r)$. The linear trend with radius reflects the fact that toroidal fields have a relatively stronger line-of-sight component the further one is from the axis. The Faraday depth tends to level off at the extremes as the integrated path length through the cylinder becomes smaller. If either the electron density or magnetic field strength strengthen off-axis, as in jet models with sheaths experiencing shear (Laing & Bridle 2014; Wang et al. 2023), these patterns would change. Note that these models simply provide consistency checks, not a unique determination of the field structure.

Because M87's jet changes structure along its length, on scales $\geq 10''$, we split up our visualizations to look at a series of cross sections, each 9.5" long, and displayed individually in (Y, Φ) space (Figure 16). Only regions 6-10 meet the full reliability criteria of Hovatta et al. (2012b) for transverse gradients. Although the signal:noise is high in regions 1-5, they are less than two beams across. Our discussion of results for regions 1-5 should be considered as suggestive, but not robust.

Cross-sections 1 and 2 correspond to Pasetto et al. (2021)'s Knot D. Although the jet is only slightly resolved transversely, it shows significant changes in Φ across the jet at these locations. The Faraday patterns here are close to the "C-shaped" poloidal example shown in Figure 15, and appears consistent with the face-on polarization data of Pasetto et al. (2021). The jet's major axis is at a position angle of $-68°$, while the magnetic field angle, using the data from Pasetto
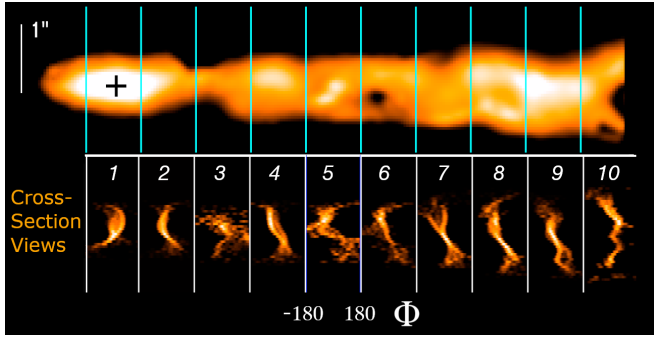
Figure 16. Section of M87 jet 9.5" long (along jet axis) by 2.5" high, at a resolution of 0.45", covering the region shown in the cyan box in Figure 14. Top: polarized intensity. Bottom: a series of ten cross sectional frames showing the polarized intensity at each value of Φ, with the vertical axis the same as the top panel. The Faraday structural patterns are to be compared with those in Figure 15. Only regions 6-10 meet the reliability criteria of Hovatta et al. (2012b) - see text. The smoothing width is 25 rad m^{-2}.

Figure 17. Polarized intensity of M87's far tail, approximately 9" long, with the location of bright Knot C marked with a cyan circle. Bottom left: View from the front. Top: the "top view" showing the Faraday depth as a function of position along the jet (matched to bottom left axis along the jet. Bottom right: "Side view" looking down the axis of the jet, position transverse to the jet, matched to the bottom left frame. The smoothing width is 25 rad m^{-2}.

et al. (2021) is $-62.5°$; the component of the field, then, projected onto the sky, is consistent with being poloidal, i.e., along the jet. This is the first evidence, to our knowledge, of 3D evidence for a jet poloidal field.

Cross-sections ([4], 6, 8, 9) show the clear tilted linear structure of toroidal (helical) fields. This is consistent with the Pasetto et al. (2021) double-helix structure, which we now detect in the third (Φ) dimension. In addition, Pasetto et al. (2021) found that the synchrotron emission itself showed the double-helix structure, along with the expected alignment of the magnetic field with the helices, in the plane of the sky.

We turn briefly to M87's far jet, the $\sim 9''$ region past Knot C (Fig. 17). Here, the jet goes through a sharp bend (Owen et al. 1990), and there are large excursions in the Faraday depth (Fig. 14). The "top view" in Fig. 17 shows the *residual* Φ along the jet, i.e., after removal of the median variations. In most locations, the jet has a finite Faraday width, indicating the presence of variations *across* the jet. In the "side view," we find that the emission is dominated by a clear, monotonic gradient in Φ across the jet, the signature of a toroidal/helical field, as shown in Fig. 15. There are also irregular enhancements in brightness along the upper and lower edges in the top view of the far jet, as would occur for a double helical structure. This is a new finding, since the earlier work (Pasetto et al. 2021) detected helical structures only in the conical region of the jet, nearer the AGN.

Other regions, as indicated by the vertical yellow lines in Fig. 17, show little variation in Φ across the jet. All of the above initial findings suggest useful further work, e.g., considering additional jet components, the effects of resolution, and smearing in Faraday space due to finite signal:noise, as well as physical modeling of the evolution of jets with double-helix structures.

4 DISCUSSION

With the rapid growth in Faraday mapping from SKA precursors, and the SKA itself, the number of well-resolved, sufficiently sensitive maps will expand dramatically, and thus the opportunity to exploit more powerful diagnostic techniques than have been previously available.

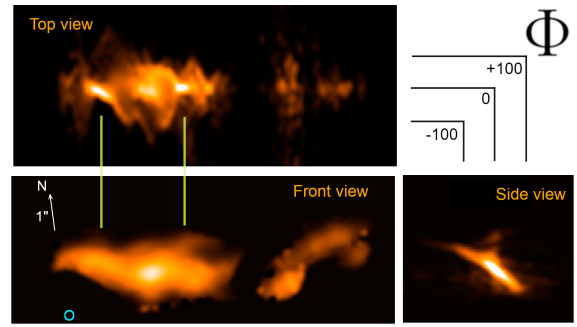We have demonstrated that a wide range of science can be studied

using $\mathbb{P}$, and that it can test or constrain simple idealized models for the structure and interactions of the thermal plasma that is adjacent to or mixed with the synchrotron plasma. Full Faraday synthesis cubes, $\mathbb{F}$(RA, Dec, Φ), can also be viewed in 3D, and offer some of the same diagnostic power (Rudnick et al. 2022), although they may come at the expense of increased complexity. $\mathbb{P}$ also offers an advantage over $\mathbb{F}$ in terms of resolving Faraday space variations; for full $\mathbb{F}$ cubes, the resolution is set by the width of the Faraday restoring beam (see Rudnick & Cotton 2023), whereas for $\mathbb{P}$, the resolution can be chosen to more closely reflect the accuracy of Φ in each pixel; see Appendix A. Current and future polarization mapping programs, such as POSSUM (Gaensler et al. 2010), VLASS (Lacy et al. 2020), MIGHTEE-POL (Taylor et al. 2024) and Apertif (Adams et al. 2022) should routinely make use of $\mathbb{P}$.

In addition, $\mathbb{P}$ can be used to exploit the extensive information on Faraday variations already in the literature, where only 2D images are available. We thus recommend that $\mathbb{P}$ analyses be applied to all existing and accessible pairs of polarized intensity and rotation measure maps, wherever there are a large number of independent spatial beams in both maps, and where the Φ variations are clearly detectable above the scatter due to noise.

Beyond the specific science use cases presented here, the most important aspect of $\mathbb{P}$ is its use as an *exploratory* tool. As we initially experimented with this new technique, we did *not* target the specific science objectives in the use cases, such as filaments or jet orientation. Instead, the science use cases are what *emerged* from our unguided examination of the movies, and it is likely that broad application of $\mathbb{P}$ will uncover other, important science questions.

The major challenge in using $\mathbb{P}$ is that it does not provide objective or robust measurements of physical parameters, nor a quantitative way to distinguish between unrelated foregrounds and local effects. In the remainder of this section, we use what we've learned so far to suggest the most useful areas for further development.

4.1 Algorithm development

The most basic need is for an algorithm to objectively distinguish between unrelated Faraday foregrounds and those associated with the emitting source. Unrelated foregrounds are present for all sources, from the Milky Way at the very least. In some science use cases, one must remove the mean foreground Faraday depth, for which all-sky Φ maps such as those of Hutschenreuter et al. (2022) can be

used.[6] The number of background sources suitable for this purpose will be dramatically enhanced with the POSSUM Survey RM Grid (Vanderwoude et al. 2024).

More detailed information on the *local* thermal plasmas comes from studying the *variations* in Faraday depth across the source. To study these local effects, the Faraday depth variations in the foreground *on the scale of the source structures* must be small with respect to the local variations. Fortunately, the Faraday scatter from the Milky Way on ~arcminute scales can be quite small. In the POS-SUM Pilot I fields centered at $b = 341.7°, l = -44°$, Vanderwoude et al. (2024) found a median Φ difference of only ~ 3 rad m^{-2} between sources with polarized fractions above 3% up to separations of 15′. Most radio galaxies are much smaller than this, although nearby sources with a great deal of Faraday structure, such as Fornax A studied here, are more likely to have significant Galactic contributions. For these larger sources, future investigations such as calculating the Pearson correlation coefficient of polarized intensity with the Galactic and extra-galactic emission, or examining gradients of the total intensity and their correlation with the total or gradients in the observed polarized intensity and Faraday structures could be useful.

However, even if the sources under study are small, or if some reduction in Galactic foregrounds can be made by masking out HII regions, or star-formation activity, there can be other unrelated foregrounds, such as the intervening intracluster medium. Our approach to identifying likely foregrounds was subjective, and this must be put on a firmer, more quantitative basis. Developments are necessary both for completely blind approaches, e.g., statistical correlations between the synchrotron and Faraday structures, as well as approaches based on radio galaxy models, as mentioned briefly below.

Algorithms are also needed to more robustly identify when variations along the line of sight, (as opposed to e.g., local $n_e B$ enhancements from the intervening molecular disk of Cen A) dominate the local Faraday structure. Here, we used the presence of coincident bending of the structure in the plane of the sky and in Faraday space in 3C40B, to argue for line of sight changes. A more convincing case could be made for repeated structures, such as the suggestion of Faraday variations for "corkscrew" tails (Fig. 3 in Johnston-Hollitt et al. 2015).

We note that automated algorithms, including the use of machine learning, and perhaps even artificial intelligence techniques, likely have an important role to play in the future of these studies. This is especially important as the data volume increases dramatically. A much more sophisticated understanding of the observational signatures of different realistic physical structures is a pre-requisite.

4.2 Visualization development

A major part of the visualization challenge is choosing the appropriate resolution in Faraday space, as explained in Appendix A. Techniques that utilize variable resolution, depending on the local signal:noise, should be explored. Scalable precision imaging (Wilber et al. 2023), based on the unconstrained Sparsity Averaging Reweighted Analysis (uSARA) optimization algorithm (Terris et al. 2023), is one recent promising development.

The visualization techniques for $\mathbb{P}$ cubes should also be extended beyond those used here. We utilized projections, movies from various angles, and small cross-sectional cuts, but other options need to be explored. The powerful *SlicerAstro* package (Punzo et al. 2017), provides a rich set of interactive options, including transparency,

cuts through the cube with arbitrary planes, and signal:noise-based smoothing. It was developed for HI cubes, but can be used in its current form for Faraday cubes; some simple modifications would also improve this new utilization.

Finally, there needs to be appropriate ways to exploit the information in full Faraday cubes, where each spatial pixel may contain information from multiple Faraday components. Issues such as distinguishing primary from secondary peaks in the spectra, effective deconvolution techniques and the appropriate choice of the display beam resolution (see Appendix A), all need to be addressed.

4.3 Science development

The most pressing need is for simulations, and radio source modeling in general, which includes the presence of a thermal plasma mixed with the synchrotron plasma and in the immediate surroundings. Mixing needs to be explored both on macroscopic scales (e.g., synchrotron filaments embedded in a thermal plasma lobe), and on microscopic scales (e.g., mixed synchrotron/thermal jets). The sophisticated 3D polarization simulations of relativistic MHD jets by Jerrim et al. (2023), visualized with $\mathbb{P}$, are one such example.

Meenakshi et al. (2023) provide a recent example of the kind of external medium studies needed, looking at the interaction of AGN jets with a surrounding turbulent medium. Another important case is magnetic draping, such as suggested by Adebahr et al. (2019) and Guidetti et al. (2011), and explored theoretically by Pfrommer (2011). A similar situation has been explored on Galactic scales, where filaments which are moving with respect to the external gas, and can produce an arc-shaped morphology as the fields bend around the filaments (Li & Klein 2019; Tahani et al. 2019, 2022a,b). The signatures of all of these in the $\mathbb{P}$ cubes need to be explored.

Another topic to be investigated is the use of other information from the emitting source to compare with the Faraday structures. These could include total intensity structures, as well as spectral indices, polarization angles and depolarization variations.

5 CONCLUSIONS

We have presented a simple visualization technique to create Pseudo-3D cubes of Faraday structure from pairs of polarized intensity and rotation measure maps, and provided a Python tool for this purpose. Using subjective, cartoon-based models, we have illustrated how to separate Faraday variations due to foregrounds unrelated to the synchrotron emitting source from those with which the source is mixed or interacting. We have applied this to several different situations, and showed how information on local Faraday structures, 3D source structures, jet orientations and the internal magnetic field configuration of jets can be derived. We find that there are many examples where these local effects are important, and thus provide new opportunities to study radio galaxy physics, including the interactions of the relativistic and surrounding thermal plasmas. It is important to understand that any models can be used to check for consistency, but do not represent unique interpretations of the observations.

We identify a number of areas where additional work is needed to exploit the use of these Pseudo-3D cubes; these involve algorithm development to put the interpretations on a more quantitative basis, visualization development to allow more powerful exploration of the $\mathbb{P}$ cubes, and scientific development to illustrate in a more comprehensive way how thermal and relativistic plasmas could be inter-related.

We recommend that these $\mathbb{P}$ techniques be used both on past and future polarization mapping projects, to inform our understanding of

the physics of radio galaxies and their interactions with the thermal plasma mediums in which they are embedded.

DATA AVAILABILITY

The polarization maps used as input for the production of $\mathbb{P}$ are available as noted in the citations for each source, from the individual originating observatories. The $\mathbb{P}$ FITS cubes produced here will be made available by the authors upon reasonable request.

REFERENCES

Adams E. A. K., et al., 2022, A&A, 667, A38

Adebahr B., Brienza M., Morganti R., 2019, A&A, 622, A209

Anderson C. S., Gaensler B. M., Feain I. J., Franzen T. M. O., 2015, ApJ, 815, 49

Anderson C., et al., 2018a, Galaxies, 6, 127

Anderson C. S., Gaensler B. M., Heald G. H., O'Sullivan S. P., Kaczmarek J. F., Feain I. J., 2018b, ApJ, 855, 41

Anderson C. S., et al., 2021, Publ. Astron. Soc. Australia, 38, e020

Anderson C. S., et al., 2022, ApJ, 937, 45

Baidoo L., Perley R. A., Eilek J., Smirnov O., Vacca V., Enßlin T., 2023, ApJ, 955, 16

Bicknell G. V., Cameron R. A., Gingold R. A., 1990, ApJ, 357, 373

Brentjens M. A., 2011, A&A, 526, A9

Brentjens M. A., de Bruyn A., 2005, A&A, 441, 1217

Bridle A. H., Perley R. A., 1984, ARA&A, 22, 319

Burns J. O., Christiansen W. A., 1980, Nature, 287, 208

Burns J. O., Feigelson E. D., Schreier E. J., 1983, ApJ, 273, 128

Candini S., et al., 2023, A&A, 677, A4

Carilli C. L., Perley R. A., Dreher J. H., 1988, ApJ, 334, L73

Ceglowski M., Gawroński M. P., Kunert-Bajraszewska M., 2013, A&A, 557, A75

Cohen M. H., Lister M. L., Homan D. C., Kadler M., Kellermann K. I., Kovalev Y. Y., Vermeulen R. C., 2007, ApJ, 658, 232

Cornwell T. J., 2008, IEEE Journal of Selected Topics in Signal Processing, 2, 793

Cotton W. D., et al., 2020a, MNRAS, 495, 1271

Cotton W. D., et al., 2020b, MNRAS, 495, 1271

Croston J. H., et al., 2009, MNRAS, 395, 1999

Dennett-Thorpe J., Scheuer P. A. G., Laing R. A., Bridle A. H., Pooley G. G., Reich W., 2002, MNRAS, 330, 609

Dennison B., 1980, ApJ, 236, 761

Ebeling H., White D. A., Rangarajan F. V. N., 2006, MNRAS, 368, 65

Fomalont E. B., Ebneter K. A., van Breugel W. J. M., Ekers R. D., 1989, ApJ, 346, L17

Gabuzda D. C., 2021, Galaxies, 9, 58

Gaensler B. M., Landecker T. L., Taylor A. R., POSSUM Collaboration 2010, in American Astronomical Society Meeting Abstracts #215. p. 470.13

Garrington S. T., Leahy J. P., Conway R. G., Laing R. A., 1988, Nature, 331, 147

Gendron-Marsolais M. L., et al., 2021, ApJ, 911, 56

Gómez J. L., et al., 2022, ApJ, 924, 122

Govoni F., Feretti L., Murgia M., Taylor G., Giovannini G., Dallacasa D., 2003, in Bowyer S., Hwang C.-Y., eds, Astronomical Society of the Pacific Conference Series Vol. 301, Matter and Energy in Clusters of Galaxies. p. 501 (arXiv:astro-ph/0211292), doi:10.48550/arXiv.astro-ph/0211292

Guidetti D., Laing R. A., Murgia M., Govoni F., Gregorini L., Parma P., 2010, A&A, 514, A50

Guidetti D., Laing R. A., Bridle A. H., Parma P., Gregorini L., 2011, MNRAS, 413, 2525

Guidetti D., Laing R. A., Croston J. H., Bridle A. H., Parma P., 2012, MNRAS, 423, 1335

Han J. L., Beck R., Berkhuijsen E. M., 1998, A&A, 335, 1117

Hardcastle M. J., 2018, MNRAS, 475, 2768

Harwood J. J., Vernstrom T., Stroe A., 2020, MNRAS, 491, 803

Hogbom J. A., 1979, A&AS, 36, 173

Hovatta T., Lister M. L., Aller M. F., Aller H. D., Homan D. C., Kovalev Y. Y., Pushkarev A. B., Savolainen T., 2012a, The Astronomical Journal, 144, 105

Hovatta T., Lister M. L., Aller M. F., Aller H. D., Homan D. C., Kovalev Y. Y., Pushkarev A. B., Savolainen T., 2012b, AJ, 144, 105

Hutschenreuter S., et al., 2022, A&A, 657, A43

Jerrim L. A., et al., 2023, arXiv e-prints, p. arXiv:2311.12363

Johnston-Hollitt M., Dehghan S., Pratley L., 2015, in Advancing Astrophysics with the Square Kilometre Array (AASKA14). p. 101 (arXiv:1501.00761), doi:10.22323/1.215.0101

Kardashev N. S., 1962, Problems of Cosmogeny, 8, 48

Klamer I., Subrahmanyan R., Hunstead R. W., 2004, MNRAS, 351, 101

Knowles K., et al., 2022, A&A, 657, A56

Kraft R. P., et al., 2007, ApJ, 665, 1129

Lacy M., et al., 2020, PASP, 132, 035001

Laing R. A., Bridle A. H., 2013a, MNRAS, 432, 1114

Laing R. A., Bridle A. H., 2013b, Monthly Notices of the Royal Astronomical Society, 437, 3405

Laing R. A., Bridle A. H., 2014, MNRAS, 437, 3405

Laing R. A., Canvin J. R., Cotton W. D., Bridle A. H., 2006, MNRAS, 368, 48

Leahy J. P., Jagers W. J., Pooley G. G., 1986, A&A, 156, 234

Li P. S., Klein R. I., 2019, MNRAS, 485, 4509

Lopez-Rodriguez E., 2021, Nature Astronomy, 5, 604

Mahatma V. H., Basu A., Hardcastle M. J., Morabito L. K., van Weeren R. J., 2023, MNRAS, 520, 4427

Meenakshi M., Mukherjee D., Bodo G., Rossi P., 2023, MNRAS, 526, 5418

Mora-Partiarroyo S. C., et al., 2019, A&A, 632, A11

Nolting C., Ball J., Nguyen T. M., 2023, ApJ, 948, 25

Oppermann N., et al., 2015, A&A, 575, A118

Owen F. N., Eilek J. A., Keel W. C., 1990, ApJ, 362, 449

Pasetto A., et al., 2021, ApJ, 923, L5

Pedelty J. A., Rudnick L., McCarthy P. J., Spinrad H., 1989, AJ, 98, 1232

Perley R. A., Bridle A. H., Willis A. G., 1984a, ApJS, 54, 291

Perley R. A., Dreher J. W., Cowan J. J., 1984b, ApJ, 285, L35

Pfrommer C., 2011, A Pedagogical Introduction to Magnetic Draping, Kavli Institute for Theoretical Physics Program: Galaxy Clusters: The Crossroads of Astrophysics and Cosmology (January 31 - April 22, 2011). Online, id.23

Pizzo R. F., de Bruyn A. G., Bernardi G., Brentjens M. A., 2011, A&A, 525, A104

Punzo D., van der Hulst J. M., Roerdink J. B. T. M., Fillion-Robin J. C., Yu L., 2017, Astronomy and Computing, 19, 45

Quillen A. C., de Zeeuw P. T., Phinney E. S., Phillips T. G., 1992, ApJ, 391, 121

Rudnick L., Blundell K. M., 2003, ApJ, 588, 143

Rudnick L., Cotton W. D., 2023, MNRAS, 522, 1464

Rudnick L., et al., 2022, ApJ, 935, 168

Saikia D. J., 2022, Journal of Astrophysics and Astronomy, 43, 97

Saikia D. J., Jeyakumar S., Mantovani F., Salter C. J., Spencer R. E., Thomasson P., Wiita P. J., 2003, Publ. Astron. Soc. Australia, 20, 50

Sebastian B., Kharb P., O'Dea C. P., Colbert E. J. M., Baum S. A., 2019, ApJ, 883, 189

Sebokolodi M. L. L., Perley R., Eilek J., Carilli C., Smirnov O., Laing R., Greisen E. W., Wise M., 2020, ApJ, 903, 36

Shah H., Seta A., 2021, MNRAS, 508, 1371

Simard-Normandin M., Kronberg P. P., 1979, Nature, 279, 115

Stull M. A., Price K. M., D'Addario L. R., Wernecke S. J., Graf W., Grebenkemper C. J., 1975, AJ, 80, 559

Tahani M., Plume R., Brown J. C., Soler J. D., Kainulainen J., 2019, A&A, 632, A68

Tahani M., et al., 2022a, A&A, 660, L7

Tahani M., et al., 2022b, A&A, 660, A97

Taylor G. B., Inoue M., Tabara H., 1992, A&A, 264, 415

Taylor A. R., Stil J. M., Sunstrum C., 2009, ApJ, 702, 1230

Taylor A. R., et al., 2024, Monthly Notices of the Royal Astronomical Society, 528, 2511

Terris M., Dabbech A., Tang C., Wiaux Y., 2023, MNRAS, 518, 604

Ubertosi F., et al., 2023, arXiv e-prints, p. arXiv:2312.02283

Urry C. M., Padovani P., 1995, PASP, 107, 803

Vanderwoude S., et al., 2024, Prototype Faraday rotation measure catalogs from the Polarisation Sky Survey of the Universe's Magnetism (POSSUM) pilot observations (arXiv:2403.15668)

Wang J.-S., Reville B., Mizuno Y., Rieger F. M., Aharonian F. A., 2023, MNRAS, 519, 1872

Wernecke S. J., D'Addario L. R., 1977, IEEE Transactions on Communications, 26, 351

Wilber A. G., Dabbech A., Jackson A., Wiaux Y., 2023, MNRAS, 522, 5558

van Breugel W., Fomalont E. B., 1984, ApJ, 282, L55
van Breugel W., Heckman T., Miley G., 1984a, ApJ, 276, 79
van Breugel W., Heckman T., Butcher H., Miley G., 1984b, ApJ, 277, 82
van Breugel W., Filippenko A. V., Heckman T., Miley G., 1985, ApJ, 293, 83
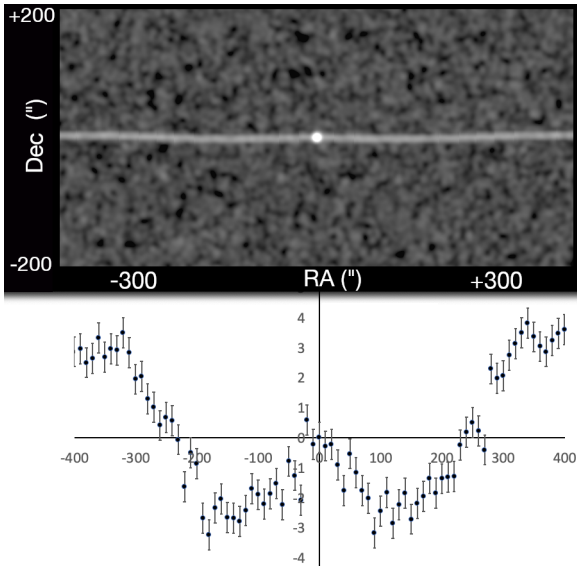van Haarlem M. P., et al., 2013, A&A, 556, A2

Figure 18. A simulated core and jets, with wiggles along the jets that are much less than its width, as described in the text. Barely visible in the greyscale (top), the wiggles are detected with high signal:noise in the Gaussian fits (bottom); errors represent the statistical error in the mean positions.

APPENDIX A: THE DISPLAY CHALLENGE

As is well known, restoring an image with a clean beam in normal radio interferometry frequently obscures the accuracy, $\delta\theta$,[7] of a feature's position. $\delta\theta$ is often less than even the pixel size. Attempts to reflect the actual positional accuracy of features include maximum entropy reconstructions (Wernecke & D'Addario 1977), and adaptive smoothing (Ebeling et al. 2006) for X-rays. Multi-resolution clean algorithms (Cornwell 2008) also have a variable effective resolution depending on brightness and the new *uSARA* algorithm (Terris et al. 2023) holds great promise. In this section, we use the term *display beam* to designate what is used for imaging, to explicitly distinguish it from the FWHM of the synthesized beam.

Figure 18 illustrates the issue. The two dimensional picture shows two jets with a signal:noise of 15; they could be straight, or have wiggles that are either symmetric or anti-symmetric. The beamwidths of both the synthesized beam and the display beam are $10''$, while the jet has transverse oscillations of only $\pm 3''$. In the 2D image, some curvature is just visible, but any possible symmetry or anti-symmetry is unclear. However, Gaussians fit to transverse profiles across the jets and a plot of the offset of their peaks (Fig. 18 bottom), show the offsets and symmetry at very high significance.

The same problem occurs in Faraday synthesis mapping, where the accuracy $\delta\Phi$ of a component's peak Faraday depth can be much smaller than the Faraday beam width or even the spectrum sampling width. In standard practice to date, the Faraday "display beam" is taken to be the width of the main peak in the Faraday amplitude spectrum (Brentjens & de Bruyn 2005).[8] Fine-scale reliable variations in the peak of the Faraday spectrum, and in the 2D images (RA, Φ) and (Dec, Φ) can be obscured if we use the nominal, and even the full resolution beam.

Figure 19. Five juxtaposed (RA, Φ) maps of the NE lobe of Cen A for different display beam sizes, listed in rad m^{-2}.

In this paper, we made a somewhat arbitrary choice of the display beam width, implemented with a Faraday smoothing width, Φ_{sm}, of typically 3-5 rad/m^2; we sought to maximize the visibility of the variations without creating artifacts due to oversampling. This needs more quantitative analysis and a robust discussion in the community about how to reliably represent the full available information.

The effects of different Faraday display beam choices are shown in Fig. 19 for the northeastern lobe of the inner double of Cen A, (Case 2). The bimodal Faraday structure of the lobe, with a separation of $\lesssim 5$ rad m^{-2}, would be invisible at the nominal Faraday resolution of ~ 60 rad m^{-2} (Anderson et al. 2018a). Here, even with a display beam as large as 5 rad m^{-2}, it is easily visible. The detailed shape of the Faraday structure becomes more apparent with the smaller display beams. At the same time, in the regions of lower brightness, the faint emission breaks up into spurious narrow bands; the structure on these very fine scales is not reliable. Such features appear in a variety of situations where oversampling is present.

This is related to the broader issue of how to identify spurious structures. In reference to their Fig. 19, Rudnick & Cotton (2023) note, "... when significant Faraday variations occur within a spatial beam, spurious structures can appear in the tomography images [images at different Faraday depths, as in the pseudo-3D cubes here]." Some signatures of spurious features include the parallel bands mentioned above, spatially unresolved jumps in Faraday depth, and the presence of significant depolarization, which indicates the presence of multiple Faraday components at the same location. Again, these visual impressions need to be investigated quantitatively, and algorithms for choosing appropriate display beam widths and recognizing spurious structures need to be developed.

---

[7] $\delta\theta = FWHM/(2 \times S/N)$ where FWHM is the clean beam size and S/N is the signal to noise ratio.

[8] Rudnick & Cotton (2023) have shown that reliable information from the complex Faraday spectra can be revealed using the narrower width of the real component of the spectrum ('full resolution').
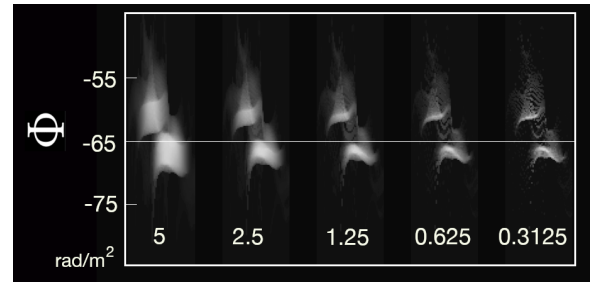
APPENDIX B: PSEUDO-3D SCRIPT AND USAGE NOTES

We provide a Python script, *generate_pseudo3D.py*, to facilitate the creation of pseudo-3D cubes. It is available at GITHUB. The script takes pairs of matched polarized intensity, Faraday depth maps and creates a pseudo-3D cube, $\mathbb{P}$. Users should first prepare the input maps to have the desired angular resolution, and optionally to mask out low polarized intensity regions. For spatially elongated structures it will also be advantageous to rotate the maps so that the major axis is either horizontal or vertical.

If a $\mathbb{P}$cube is desired for only a smaller cross section of the source, as in Fig. 16, then the simplest approach is to make an input pair of (PI,Φ) images of only that area. Alternatively, a portion of the output $\mathbb{P}$ cube can be extracted, as needed, but this must be done before visualization of the cube from different angles.

The required input parameters for *generate_pseudo3D.py* are the minimum and maximum Faraday depths to be included, the pixel size in Faraday depth, and a Faraday smoothing width. We recommend that the boundaries in Faraday depth be somewhat larger than the range of significant depths in the image, and that the pixel size and smoothing width be guided by the considerations in Appendix A.

For visualization, we used *SAOimage DS9* in 3D Frame mode to view the cube from different directions. We used Average Intensity Projection (AIP) rendering, and then created movies using $1°$ viewing angle increments back and forth over $90°$, typically around the major axis. Zooming in on the Φ axis is often useful, and is accomplished in *DS9* using the 3D Frame parameter *Z Axis Scale*. We also strongly recommend investigations using the interactive package *SlicerAstro*, (Punzo et al. 2017). It has a steep learning curve but offers a large number of additional tools, such as transparency and slicing of the cube.

We note again that $\mathbb{F}$ cubes created from the full Faraday spectrum at each pixel are similar to "pseudo-3D" cubes in that the Faraday axis may or may not correspond to the actual third spatial dimension. Movies of $\mathbb{F}$ cubes can also be useful, but are at a much lower resolution than $\mathbb{P}$ cubes and subject to confusion from emission away from the main peak.